Modeling of Terahertz Attenuated Total Reflection Experiments

L.W. Weber[1], Y. Li[2], and R. Valdes Aguilar[2]

[1]*Department of Physics, Southern Illinois University-Carbondale, and the Center for Emergent Materials, Ohio State University*
[2]*Department of Physics, Ohio State University*

Abstract: In this study we model various attenuated total reflection spectroscopy experiments to find the experimental signatures of magnetic polaritons in antiferromagnets. Isotropic materials and two-sublattice uniaxial antiferromagnets are discussed. Our simulations reveal that bulk and surface magnetic polariton modes can be observed in these antiferromagnets, and they also provide information about important experimental considerations for attenuated total reflection experiments.

Section I: Introduction

Magnetic Materials and the Terahertz Frequency Range

In some materials, it is possible for different groups of atoms to spontaneously arrange themselves into distinct magnetic sublattices, where the spins of each atom in a sublattice are all oriented in the same direction. Antiferromagnets in particular have multiple magnetic sublattices with the spins of each sublattice oriented antiparallel to each other, resulting in zero net magnetization. Antiferromagnets also have a magnetic resonance frequency, which is typically dependent on the magnetic field applied to the material, material properties such as the exchange and anisotropy fields, and the relative orientation of the applied magnetic field and the crystal lattice [1]. In order to extract information from spectroscopic experiments about the properties of magnetic materials, including antiferromagnets, it is often necessary to use radiation of a frequency close to their magnetic resonance. Many antiferromagnets have magnetic resonances in the range of a few terahertz (THz) (1 THz=10^{12} Hz) [2,3], which makes THz radiation an ideal tool for studying the magnetic properties of antiferromagnets. In this study, we will simulate the interactions of a THz probe with various types of antiferromagnets.

Magnons are magnetic quasiparticles sometimes referred to as “spin waves” – collections of oscillations of the spins of neighboring atoms that create a wave-like structure. Naturally, these particles have a characteristic frequency. When light of a similar frequency comes near a magnon, a magnetic polariton can be created – the combination of a photon coupled to a magnon [4]. From a fundamental standpoint, one of the reasons that it is interesting to study antiferromagnets is to learn about the behavior of magnon and polariton states that may exist in them.

The general focus of our modeling is to simulate an experiment that can probe antiferromagnetic materials using terahertz radiation, and that can detect signatures of magnetic polaritons in these materials. Specifically, we aim to simulate an experiment that can detect and characterize surface magnetic polariton states in antiferromagnets.

The Permittivity and Permeability Tensors

The electric permittivity and magnetic permeability of isotropic materials are related to the permittivity and permeability of free space by their relative permittivity ε_r and relative permeability μ_r. For anisotropic materials, however, we must instead use the permittivity and permeability tensors $\overleftrightarrow{\boldsymbol{\varepsilon}}$ and $\overleftrightarrow{\boldsymbol{\mu}}$. These tensors are typically 3x3 matrices that relate the electric or magnetic field and flux density by Equations 1.1 and 1.2 [5]:

$$\boldsymbol{D} = \vec{\boldsymbol{\varepsilon}}\boldsymbol{E} \tag{1.1}$$

$$\boldsymbol{B} = \vec{\boldsymbol{\mu}}\boldsymbol{H} \tag{1.2}$$

For the purposes of this study, we will assume that the permittivity tensor is simply an identity matrix multiplied by the isotropic permittivity (though this is not necessarily true). We will instead focus on the magnetic properties of antiferromagnets, expressed by their permeability tensor. The permeability tensor of antiferromagnets is frequency-dependent and can contain off-diagonal terms under certain circumstances – for example, if an external magnetic field is applied [6]. The form of this tensor will be discussed further in Section II.

Attenuated Total Reflection

One technique that can be useful for characterizing magnetic materials is attenuated total reflection (ATR). Figure 1.1 shows a schematic that illustrates the working principle of this experiment. An electromagnetic wave enters a triangular prism and reflects off the bottom surface. Under the prism is a gap (a vacuum or some other material) with an index of refraction lower than the index of the prism. There is some critical angle θ_c between the incident light and the normal (marked with a dashed line) above which the light will be totally internally reflected, and it can be found using Snell's law [7]:

$$n_p \sin[\theta_p] = n_g \sin[\theta_g] \tag{1.3}$$

$$\theta_p = \sin^{-1}\left[\sin[\theta_g]\,\frac{n_g}{n_p}\right] \tag{1.4}$$

Where n_p and n_g are the refractive indices of the prism and the gap, respectively, and θ_p and θ_g are the angles between the light and the normal in the prism and the gap. To find the critical angle, we say that $\theta_g = \frac{\pi}{2}$ and $\theta_p = \theta_c$, so Equation 1.4 becomes:

$$\theta_c = \sin^{-1}\left[\frac{n_g}{n_p}\right] \tag{1.5}$$

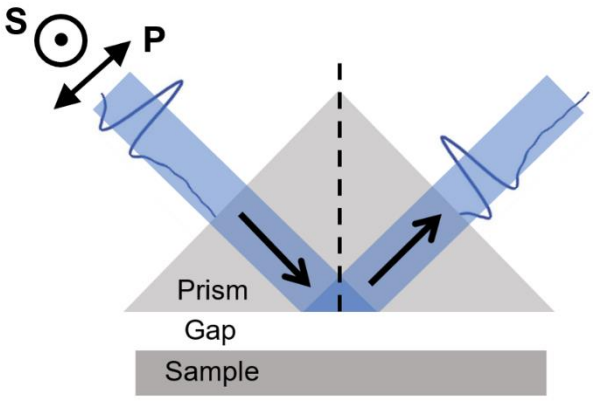

Figure 1.1: Schematic of a typical ATR experiment

Above this critical angle, and with only a vacuum (and no sample) below the prism, the energy of the reflected wave will always equal the energy of the incident wave. However, if a sample is introduced below the prism, the evanescent wave created during the total internal reflection can interact with the sample, and this can cause the reflected wave to have less energy than the incident wave (it is attenuated) [3,6]. The evanescent wave propagates only a short distance below the prism, so the sample must be very close to observe this effect (in the order of 10-100 μm). The signal typically collected from this experiment is the reflectivity R of the electromagnetic wave, which we define as:

$$R = |r|^2 \tag{1.6}$$

Where r is the complex reflection coefficient. By measuring the reflectivity for different frequencies of light, different gap distances between the prism and the sample, and by varying other experimental parameters, this experiment can produce data that can be useful for the study of magnetic properties of materials, or for other types of characterization [6,8,9].

Our calculations here are done for s-polarized (electric field perpendicular to the plane of incidence) and p-polarized (E-field in the plane of incidence) incident light. The electric field directions for these polarizations are shown in Figure 1.1. For many experimental configurations and materials, the reflected light will be of the same polarization as the incident light (i.e., s-polarized incident light will produce reflected s-polarized light). However, in some cases, and particularly for anisotropic materials, it is possible that s-polarized incident light can create p-polarized reflected light, and vice versa. We call a reflection with incident s-polarized light and reflected p-polarized light "s-p"; if the incident and reflected light are both s-polarized, it is "s-s", and similar notation is used for p-p and p-s reflections [6].

In order to analyze the reflected light, we must solve Maxwell's equations for each of the waves present inside each material in Figure 1.1. It can be demonstrated that the wavevector of each of these waves is related to the eigenmodes of their magnetic fields by the following equations [10], using the Einstein summation convention and the Levi-Civita symbol ϵ_{ijk}:

$$\left(\epsilon_{ijk}\boldsymbol{k}_j[\vec{\vec{\boldsymbol{\varepsilon}}}^{-1}]_{kl}\epsilon_{lmn}\boldsymbol{k}_m + \omega^2\,\vec{\vec{\boldsymbol{\mu}}}_{in}\right)\boldsymbol{H}_n = \boldsymbol{0} \tag{1.7}$$

This equation simplifies when all materials involved are isotropic:

$$(\boldsymbol{k}\boldsymbol{k}^T - \boldsymbol{k}^T\boldsymbol{k}\boldsymbol{I}_3 + \omega^2\varepsilon\mu\boldsymbol{I}_3)\boldsymbol{H} = \boldsymbol{0} \tag{1.8}$$

Once we solve this equation to find all the wavevectors and eigenmodes of the electric and magnetic fields, we can solve for the magnitudes of the incident and reflected electric fields using Maxwell's equations and boundary conditions applied at the bottom surface of the prism and the top surface of the sample, as pictured in Figure 1.1 [10]. After that, the calculations to find the reflectivity are straightforward.

These quantities are solved for the incident and reflected wave inside the prism, but the electric field magnitudes we found could be easily used to find those quantities outside the prism with the application of the Fresnel equations in the following form [7]:

$$t_s = \frac{2n_i\cos[\theta_i]}{n_i\cos[\theta_i] + n_t\cos[\theta_t]} \tag{1.9}$$

$$t_p = \frac{2n_i\cos[\theta_i]}{n_i\cos[\theta_t] + n_t\cos[\theta_i]} \tag{1.10}$$

Where t_s and t_p are the transmission coefficients of s- and p-polarized light entering the prism, θ_i and θ_t are the angles of incidence and transmission, and n_i and n_t are the indices of refraction of the material outside the prism and the prism, respectively. These transmission coefficients could be easily calculated using the design of the experimental setup. It not incorporated into our simulations for simplicity, but it would need to be considered for a model of experimental data.

Section II: Results of Simulations

Isotropic Materials

For all of these simulations, we assume that the gap is vacuum, and that the prism is made of pure silicon. We chose silicon because it is mostly transparent to radiation in the THz regime and because its index of refraction allows us to use an angle of incidence of $\theta = \frac{\pi}{4}$, which is convenient for experiments [11].

Let's first consider an ATR experiment with a silicon prism, a vacuum gap, and an isotropic sample with an index of refraction n. The angle of incidence is $\frac{\pi}{4}$ from the normal, and the incident radiation

is monochromatic, with an arbitrary frequency of 1 THz (the behavior discussed here is the same for any frequency in the range of 0.1-10 THz, and we do not consider magnetic resonances for isotropic samples). The results concern the reflectivity (as defined in Equation 1.6) of our setup as a function of the gap distance (d, the distance between the sample and the prism in Figure 1.1). These plots are given in Figure 2.1 and 2.2. The first thing that should be noted is that the s-p and p-s reflectivity are zero, as we expect for an isotropic material [10]. The s-s and p-p reflectivities are plotted here for multiple values of n – Figure 2.1 contains values of n from 2.5 to 3.42 (the refractive index of silicon) and Figure 2.2 contains values from 3.42 to 20. Lower indices of refraction are not used because at approximately $n = 2.41$, the reflectivity of any polarization goes to 1 for all distances (indicating that experimentally there would be no signal). At high distances ($d \approx 50\,\mu m$), both the s-s and the p-p reflectivities approach 1. This is expected because the angle of incidence $\frac{\pi}{4}$ is sufficient for total internal reflection to take place when there is no sample for the evanescent wave to interact with. Furthermore, when $n = 3.42$ (the sample has the same refractive index as silicon), the reflectivities approach zero at $d = 0\,\mu m$. This is necessary because under those circumstances the experiment simplifies to an electromagnetic wave entering a continuous block of silicon.

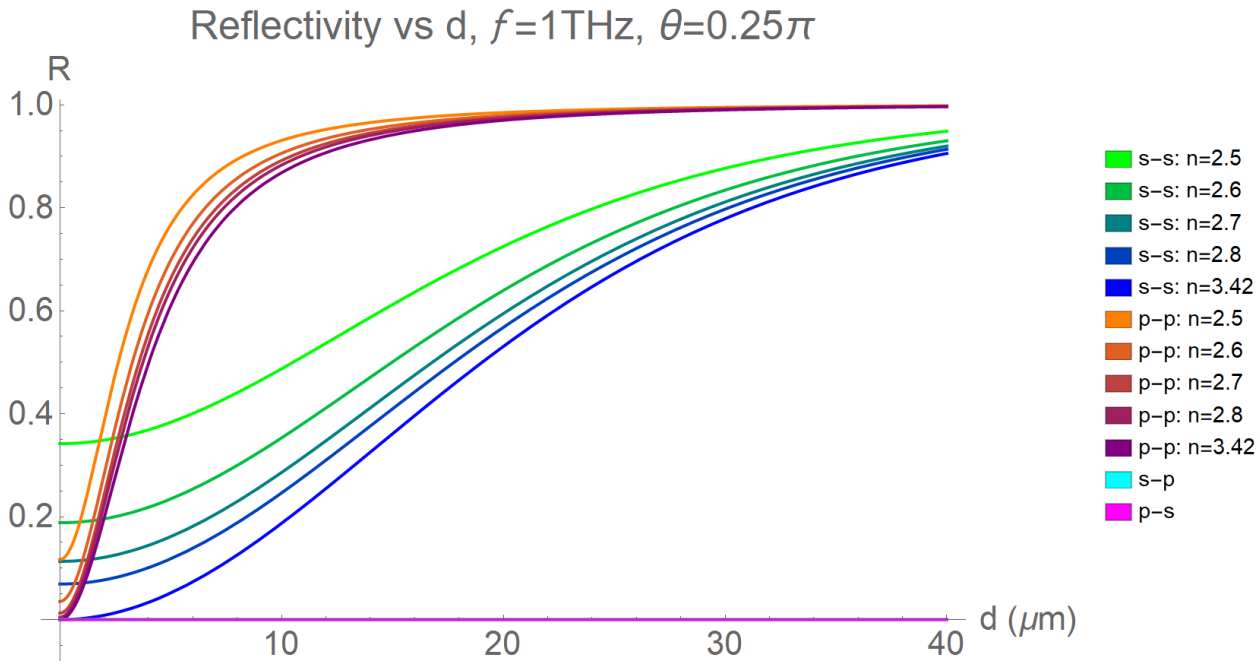

Figure 2.1: Reflectivity vs gap distance for various polarization combinations and indices of refraction below 3.42. The angle of incidence is $\theta = \frac{\pi}{4}$ and the incident light has frequency f = 1 THz.

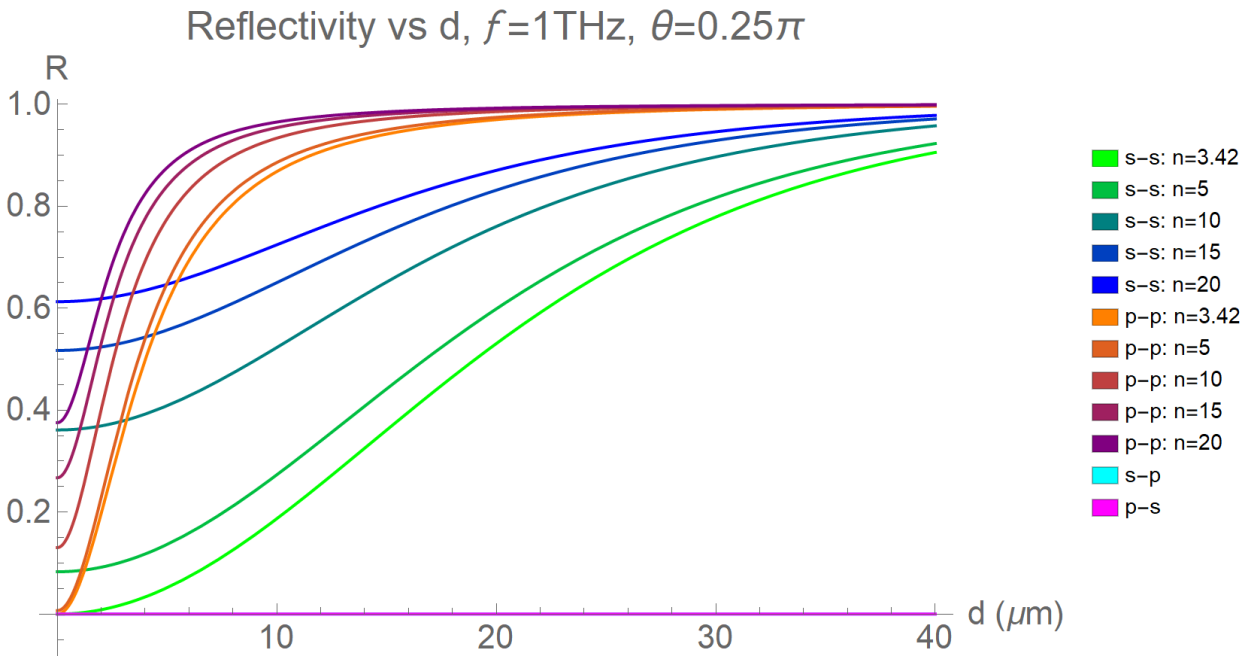

Figure 2.2: Reflectivity vs gap distance for various polarization combinations and indices of refraction above 3.42. Experimental conditions are the same as those of Figure 2.1.

Two-Sublattice Uniaxial Antiferromagnets

Next, we move on to antiferromagnets. We will again assume for our calculations that the prism is made of silicon and that the gap between the prism and the sample is vacuum. We consider in this report antiferromagnets with two magnetic sublattices and a single easy axis parallel to the surface of the sample. We must first calculate the frequency-dependent permeability tensor $\vec{\vec{\mu}}$ for our sample, which requires a few material properties, the relative orientation of the easy axis and the externally applied magnetic field, and a generalized damping constant Γ included by the substitution $\omega = \omega + i\Gamma$. The damping constant is primarily related to the temperature of our sample, so from this point forward we consider low-temperature (~20 K) measurements because they are necessary to lower the damping constant Γ enough to collect a usable signal [6]. For a simple two-sublattice uniaxial antiferromagnet, the permeability tensor takes the form:

$$\vec{\vec{\mu}}(\omega) = \begin{bmatrix} \mu_{xx} & \mu_{xy} & 0 \\ \mu_{yx} & \mu_{yy} & 0 \\ 0 & 0 & \mu_{zz} \end{bmatrix} \mu_0 \qquad (2.1)$$

The expressions for each matrix-element term in Equation 2.1 are given for multiple experimental configurations in reference [6]. For the special case of a two-sublattice uniaxial antiferromagnet with the easy axis and the applied magnetic field oriented in the same direction and parallel to the surface, the terms take the following form:

$$\mu_{xx} = \mu_{yy} = 1 + 4\pi\gamma^2 H_A M_S (Y^+ + Y^-) \quad (2.2)$$

$$\mu_{xy} = -\mu_{yx} = 4i\pi\gamma^2 H_A M_S (Y^+ - Y^-) \quad (2.3)$$

$$\mu_{zz} = 1 \quad (2.4)$$

Where $Y^{\pm} = (\omega_r^2 - (\omega \pm \gamma H_0)^2)^{-1}$. H_A is the anisotropy field, M_S is the sublattice magnetization, γ is the gyromagnetic ratio, and ω_r is the bulk magnetic resonance frequency. If there is no applied field, the off-diagonal terms become zero and there is one resonance frequency. However, as the applied field H_0 increases, two resonance frequencies emerge and move farther apart with greater field. This is typical of antiferromagnets; a sample antiferromagnetic resonance frequency plot is given in Figure 2.3. If the easy axis is instead aligned perpendicular to the magnetic field, the μ_{zz} term is no longer one, and it has a different resonance frequency than the other terms.

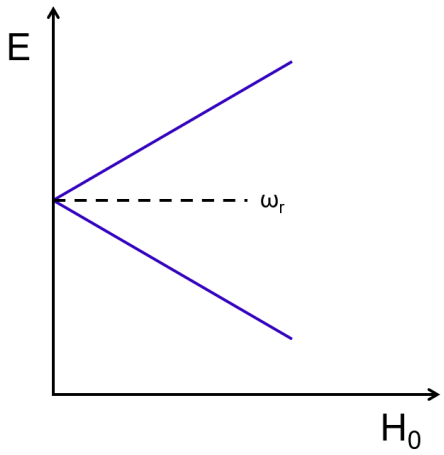

Figure 2.3: Typical antiferromagnetic resonance frequency plot. ω_r is the zero-field resonance frequency.

Note that in Equation 2.1, the axes conventions are defined so that the y-axis is normal to the surface of the sample. To rectify this, we must apply a transformation to the tensor, so that in accordance with our geometry given in Figure 2.4, the permeability tensor takes the form [2]:

$$\overleftrightarrow{\boldsymbol{\mu}}(\omega) = \begin{bmatrix} \mu_{xx} & 0 & \mu_{xz} \\ 0 & \mu_{yy} & 0 \\ \mu_{zx} & 0 & \mu_{zz} \end{bmatrix} \mu_0 \quad (2.5)$$

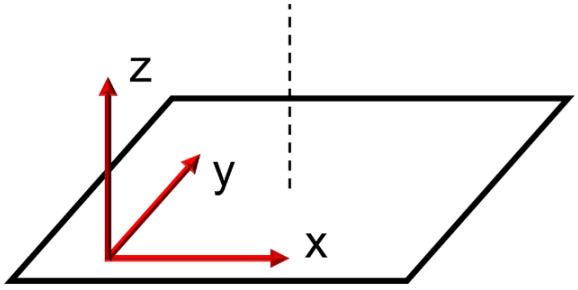

Figure 2.4: Experimental geometry. The z-axis is normal to the surface of the sample (pictured), H0 is applied in the y-direction, and the easy axis is in the xy-plane.

This geometry is defined by the normal axis (z) and the direction of the applied magnetic field (y). For this report we will consider only experimental configurations with the easy axis of the sample and the applied magnetic field aligned parallel to the sample surface.

For the initial calculations on uniaxial antiferromagnets, we are interested primarily in their polariton signatures in reflectivity measurements. Sample reflectivity curves are calculated for the frequently studied two-sublattice uniaxial antiferromagnet FeF_2. The lattice structure of FeF_2 (which is body-centered tetragonal) is pictured in Figure 2.5. The blue spheres represent iron atoms with spin up, and the red spheres represent iron atoms with spin down. These groups form two magnetic sublattices, with the easy axis oriented as shown [1]. Calculated reflectivity curves for FeF_2 are given in Figures 2.6 and 2.7. For these figures, the easy axis is aligned in the same direction as the applied magnetic field,

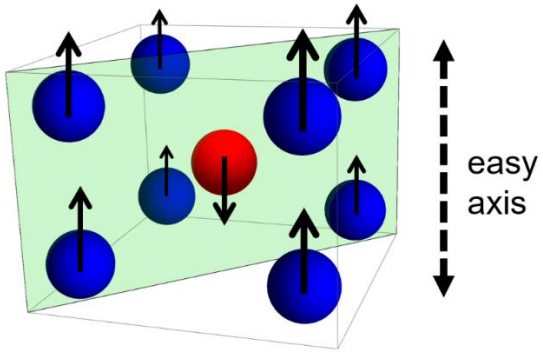

Figure 2.5: Lattice structure of the two-sublattice uniaxial antiferromagnet FeF_2. The magnetic sublattices are shown in blue (spin up) and red (spin down).

and the plane of incidence is perpendicular to that axis (it is the xz-plane in Figure 2.4). Only s-s reflection is considered at this time. From Figures 2.6 and 2.7 we can observe the changes in the calculated reflectivity signal for various values of the damping constant Γ, the gap distance d, the angle of incidence with respect to the normal θ, and the applied magnetic field H_0.

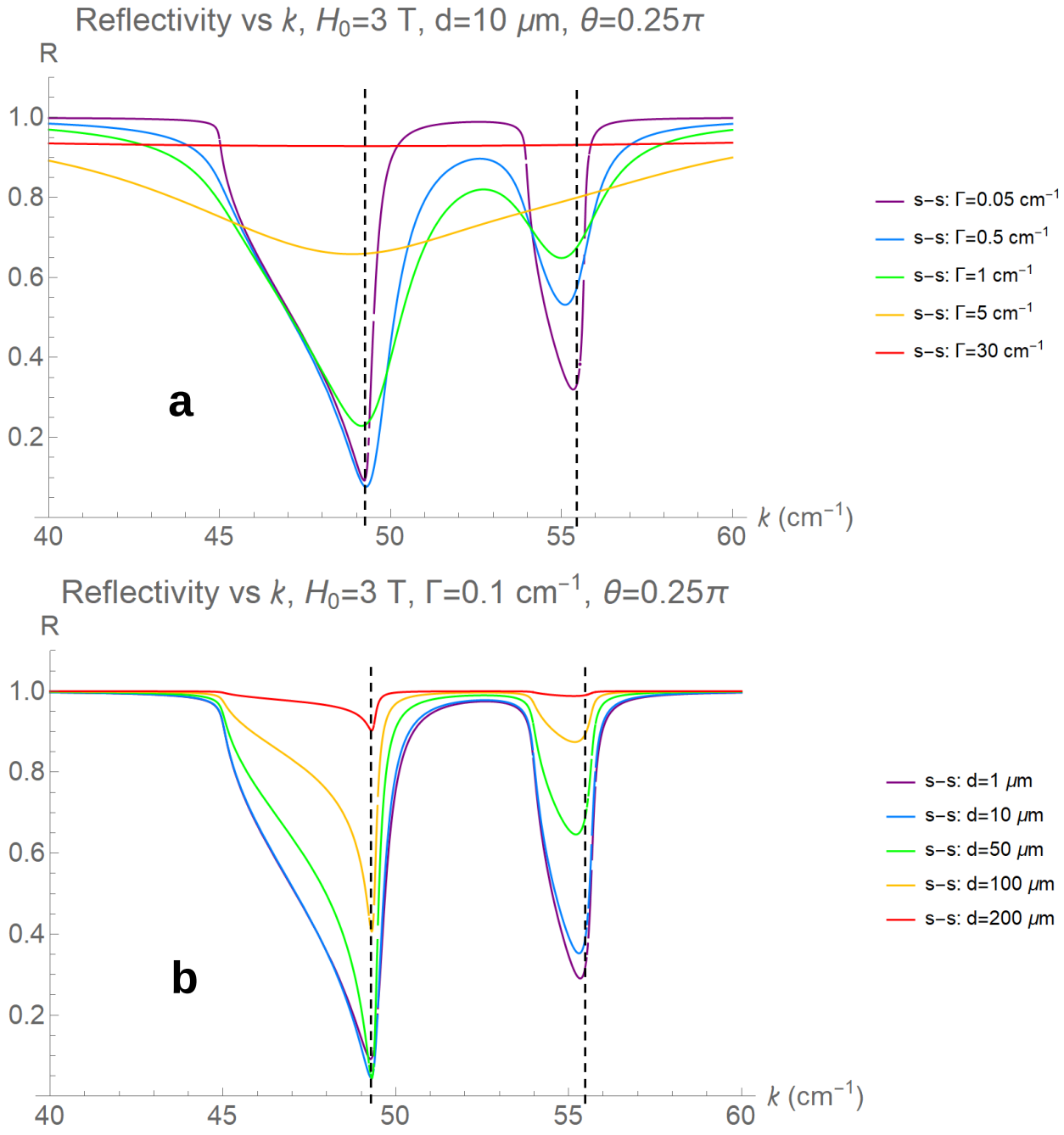

Figure 2.6: s-s reflectivity vs wavenumber with varying a) damping constant, and b) gap distance. The applied magnetic field is 3T and the angle of incidence is $\frac{\pi}{4}$, with a) $d = 10\ \mu m$, and b) $\Gamma = 0.1\ cm^{-1}$. The easy axis and the applied magnetic field are parallel to each other and to the surface, and they are both perpendicular to the plane of incidence. The resonance frequencies are marked with dashed lines.

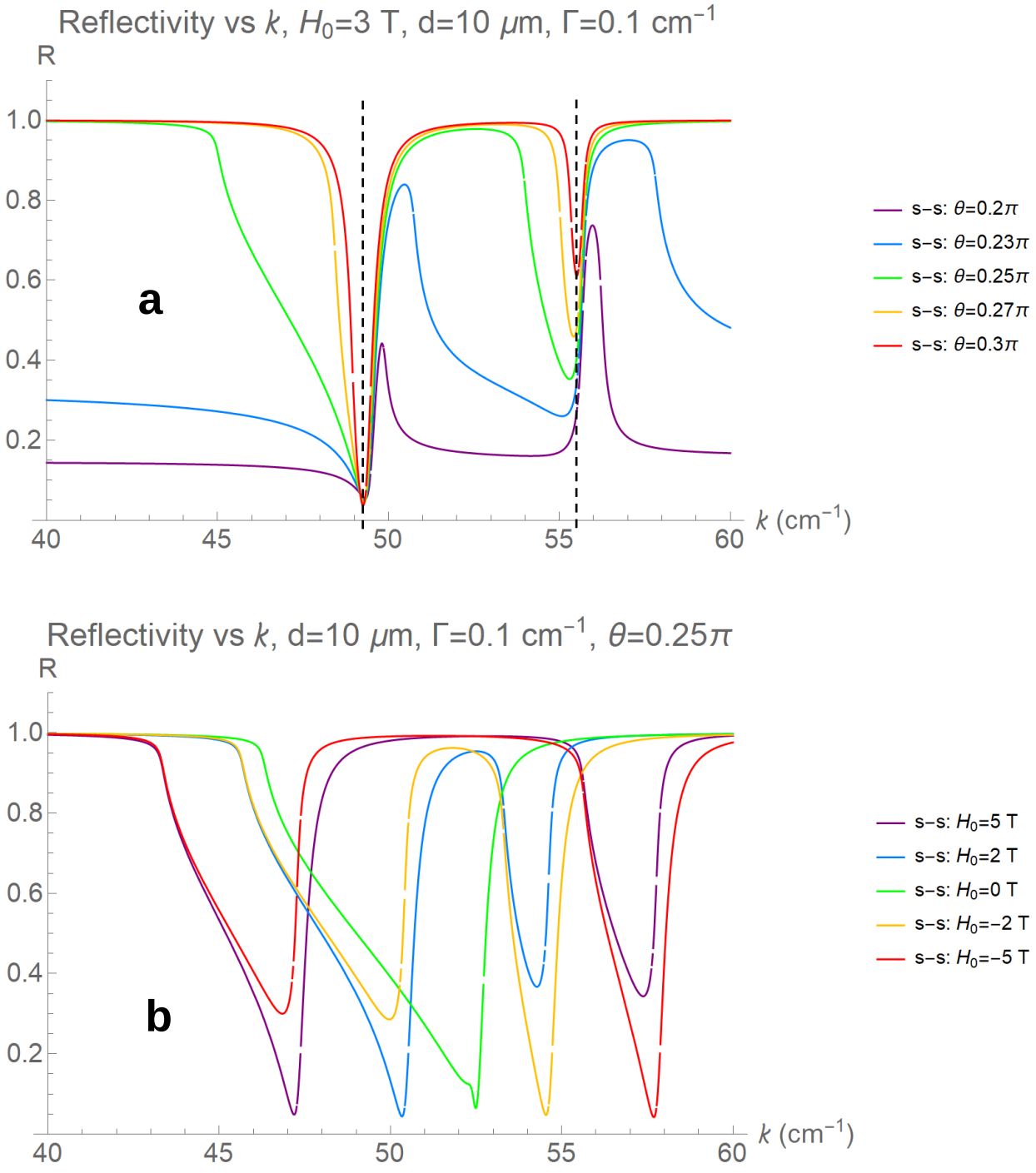

Figure 2.7: s-s reflectivity vs wavenumber, with varying a) angle of incidence, and b) applied magnetic field. The gap distance is 10 μm and the damping constant is 0.1 cm^{-1}, with a) $H_0 = +3\ T$, and b) $\theta = \frac{\pi}{4}$. The easy axis and the applied magnetic field are parallel to each other and to the surface, and they are both perpendicular to the plane of incidence. The resonance frequencies are marked with dashed lines.

Section III: Analysis and Conclusions

Discussion of Results

Let's first focus on the data in Figure 2.6a. For the curve with $\Gamma = 0.05\ \mathrm{cm}^{-1}$, the resonance signal at approximately a wavenumber of 48 or 49 cm^{-1} has two distinct regions: first a smaller "depression" in the reflectivity curve, and then a sharp "dip" at $\sim k = 49.2\ \mathrm{cm}^{-1}$. This broad, shallow signature corresponds to light coupling with bulk polaritons in FeF_2, and the narrow signal corresponds to surface polaritons. This behavior is explained by the dispersion curves of FeF_2 given in [6]. Further evidence is given in Figure 2.7b, where we can observe that these polariton signatures are non-reciprocal (they are different for $+H_0$ and $-H_0$). In FeF_2, bulk polariton modes are reciprocal, but surface polariton modes non-reciprocal – the $+q$ surface polariton mode is present only at the lower-wavenumber resonance, and the $-q$ surface polariton mode is present only at the higher-wavenumber resonance [6]. In the lower-wavenumber resonance, we observe both bulk and polariton modes for the $+H_0$ measurement, but only the bulk modes for the $-H_0$ measurement. The opposite is true for the higher-wavenumber resonance.

In addition, we observe in Figure 2.7a a critical angle somewhere between $\theta = 0.23\pi$ and $\theta = 0.25\pi$ above which incident light will be totally reflected, except at the magnetic resonances. Below this angle, the incident light will only be partially reflected, and polariton signatures may be more difficult to interpret. Note that this critical angle is different than the classically defined critical angle given in Equation 1.5 that would be present without any sample.

We know that to obtain an optimal signal in an ATR experiment, we need our sample to have a low damping constant Γ and we need the ability to reach low separation distances. However, it appears that a low damping constant (most likely attained by temperatures in the range of 5-20 K [6]) is more important for this purpose than the gap distance. In Figure 2.6b, we can see that for a damping constant of $\Gamma = 0.1\ cm^{-1}$, a significant signal is visible until a separation of greater than 100 μm is reached. However, Figure 2.6a shows that the signal disappears rapidly after the damping constant reaches just a few cm^{-1}. In addition, it becomes very difficult to distinguish visually the bulk and surface polariton regions at damping constants higher than 0.5 cm^{-1}. However, they can still be identified by recognizing that in FeF_2 bulk polariton modes are reciprocal and surface polariton modes are not, and this effect is measurable even for high Γ and d values.

The curves in Figures 2.6 and 2.7 are calculated for an experimental configuration with the easy axis parallel to the applied magnetic field and to the surface of the sample. However, the permeability tensor is changed if the magnetic field is applied perpendicular to the easy axis and parallel to the surface. Under these conditions, the μ_{yy} term in Equation 2.5 has a different resonance frequency than the μ_{xx}, $\mu_{xz,}$ $\mu_{zx,}$ and μ_{zz} terms. However, in an experiment these resonances are usually too close to distinguish, and in fact with this configuration it will be difficult to observe any peak splitting at all. Extremely high magnetic fields would be required to see distinct resonances in a graph like Figure 2.7b.

Experimental Considerations

Figures 2.6 and 2.7 are important primarily because they outline the basic experimental requirements that are necessary to measure a useful ATR reflectivity signal (at least, for FeF_2 in the given experimental configuration). In an ideal experiment attempting to replicate these findings, the damping constant should be less than 1 cm^{-1}, the gap distance should be in the order of 10 μm, and magnetic fields of at least 1-2 T should be possible. In addition, the angle of

incidence should be above the critical angle mentioned earlier ($\theta = \frac{\pi}{4}$ is a good choice with a silicon prism, since it satisfies that condition and it is convenient for experiments).

In general, under these conditions and for the given sample and experimental setup, it is expected that the polariton signatures shown could be observed in an experiment. In addition, for low damping constants, it is expected that distinct bulk and surface polariton regions should be possible to observe. The non-reciprocal nature of surface polaritons could be observed at slightly higher damping constants; however, to accomplish this, the direction of the magnetic field or of the incident light would need to be reversed to probe the $+q$ and $-q$ modes visible for magnetic fields of $+H_0$ and $-H_0$, respectively.

Conclusions

We have accomplished two of the primary goals of this study, namely: developing a model that can simulate the ATR reflectivity results expected for isotropic materials and for antiferromagnets, and using this model to observe surface polariton modes in the antiferromagnet FeF_2. In addition, we have found a group of experimental guidelines that should be followed in an actual THz ATR spectroscopy experiment, although slight variances are expected for changes in sample material or in the magnetic field or easy axis orientation. Strictly speaking, the data given in Figures 2.6 and 2.7 is only valid for FeF_2 and for an experiment with the easy axis and magnetic field parallel to each other and to the sample surface, with the incident plane perpendicular to the easy axis. However, in certain cases it may be appropriate to apply these findings to similar experiments.

In that sense, this model is not yet complete. A possible direction for future development of our simulations is to expand the model for different experimental setups to include every possible geometry of the magnetic field, easy axis, and plane of incidence. We may later do these calculations for different classes of materials as well, such as easy plane antiferromagnets, antiferromagnets with more than two magnetic sublattices, or ferrimagnets.

Section IV: Acknowledgements

The authors acknowledge support from the Center for Emergent Materials at The Ohio State University and the National Science Foundation, NSF Award Number DMR-1420451.

Section V: References

[1] S.M. Rezende et. al., *Introduction to Antiferromagnetic Magnons*. J. Appl. Phys 126 (2019) 151101.

[2] F. Keffer and C. Kittel, *Theory of Antiferromagnetic Resonance*. Phys. Rev. B. 85 (1952) 329.

[3] R. Macedo and R.E. Camley, *Engineering Terahertz Surface Magnon-Polaritons in Hyperbolic Antiferromagnets*. Phys. Rev. B. 99 (2019) 014437.

[4] M.G. Cottam and D.R. Tilley, *Introduction to Surface and Superlattice Excitations*. Cambridge University Press, Cambridge, 1989.

[5] L.A. Alexeyeva et. al., *Generalized Solutions of Maxwell Equations for Crystals with Electric and Magnetic Anisotropy*. Journal of Electromagnetic Waves and Applications 28:16 (2014) 1974-1984.

[6] K. Abraha and D.R. Tilley, *Theory of Far Infrared Properties of Magnetic Surfaces, Films, and Superlattices*. Surface Science Reports 24 (1996) 125-222.

[7] B.D. Guenther, *Modern Optics*. Oxford University Press, Oxford, 2015.

[8] M. Safar et. al., *Characterization of Edible Oils, Butters, and Margarines by Fourier Transform Infrared Spectroscopy with Attenuated Total Reflectance*. JAOCS 71 4 (1994) 371-377.

[9] Y.A. Gorokhovatskiy et. al., *The Detection of Charge-Dipole Centers in Composites Based on Polylactide by Attenuated Total Reflectance Method*. 2019 IEEE International Conference of Electrical Engineering and Photonics (2019).

[10] Y. Li and R. Valdes Aguilar, Personal Communication, 2020.

[11] X. Zhang and J. Xu, *Introduction to THz Wave Photonics*. Springer, Boston, MA, 2010.